PCCP

PAPER

View Article Online
View Journal | View Issue

Cite this: *Phys. Chem. Chem. Phys.*, 2023, **25**, 9454

First-principles study on unidirectional proton transfer on anatase TiO_2 (101) surface induced by external electric fields†

Takahiro Chiba,[a] Kenji Iida, *[a] Shinya Furukawa [a] and Jun-ya Hasegawa [ab]

Received 6th February 2023,
Accepted 8th March 2023

DOI: 10.1039/d3cp00577a

rsc.li/pccp

The electric field (EF) effect on hydrogen or proton transfer (PT) *via* hydroxyl groups on an anatase TiO_2 (101) surface is examined using first-principles density functional theory and the modern theory of polarization. This study focuses on unidirectional surface PT caused by external EFs at various orientations toward the surface. The preferred PT pathway can change depending on the magnitude and direction of the EF. Detailed analysis reveals that the variation in the energy profile with the EF is significantly different from that determined by the classical electric work of an EF carrying a point charge. The EF effect on the energy profile of the PT is governed by the rearrangement of the chemical bond network at the interface between the water molecules and the surface.

Introduction

The electric field (EF) effect in solid–molecule interfaces has been extensively studied owing to the interest in manipulating surface chemical processes and understanding electrochemical reactions.[1–5] Planar solid surfaces in conventional electrocatalysts have been widely used to investigate the EF effect, and the direction of the applied EF is assumed to be perpendicular to the solid surfaces.[1,2] However, recent experimental studies have focused on controlling the EF effect in complex systems with laterally non-uniform interfaces.[3,6,7] An oriented EF generated by a scanning tunneling microscope tip was used to accelerate non-redox chemical reactions, such as the Diels–Alder reaction,[3] extending the applicability of the EF effect to control chemical processes other than electrochemical reactions. Furthermore, the EF effect on heterogeneous materials with complex interfaces has attracted increasing attention.[6,7] Catalytic activity in the dehydrogenation of hydrocarbons was improved by applying a bias voltage to a powdered catalyst, and proton transfer (PT) on the oxide surface has been considered to be enhanced by the external EF.[6,8,9] However, the EF effect on heterogeneous materials is complex because the magnitude and direction of the EFs vary in space due to EFs generated by electric polarization in the interface region; that is, the gross EFs point in various directions on the material surface. Therefore, a theoretical study is required to understand the EF effect.

Numerous theoretical and computational studies have been performed to understand solid surfaces under external EFs.[1,10–12] First-principles density functional theory (DFT) calculations with a sawtooth-type electrostatic potential have been used to calculate the effect of a surface-perpendicular external EF. However, the sawtooth potential cannot be applied when the EF is parallel to the material surface, and electronic polarization cannot be uniquely defined for periodic systems.[13,14] Therefore, an alternative to the sawtooth potential is required to investigate the EF effect on heterogeneous materials.

The Berry phase theory is used to evaluate the macroscopic polarization of periodic systems[13,14] and is applicable to the investigation of the EF effect, irrespective of the orientation of the EF toward the material surface. EF-induced electronic polarization of various dielectric materials has been investigated in condensed matter and device physics research.[15] However, the Berry phase theory has not been applied to complex chemical processes with multiple elementary steps, despite the expectation that the energy profile will change significantly with the EF.

In this study, we performed DFT calculations to investigate the EF effect on hydrogen or proton transfer *via* hydroxyl groups on an anatase TiO_2 (101) surface. Hereafter, both hydrogen and proton transfers are denoted as PT because hydrogen and protons cannot be clearly distinguished in the PT process. The interface between TiO_2 and water under an external EF has been widely studied to understand catalytic and spectroscopic properties.[9,16–18] Herein, the Berry phase theory formula is combined with an approximated

[a] *Institute for Catalysis, Hokkaido University, N21 W10 Kita-ku, Sapporo, 001-0021 Hokkaido, Japan. E-mail: k-iida@cat.hokudai.ac.jp*
[b] *Interdisciplinary Research Center for Catalytic Chemistry, National Institute of Advanced Industrial Science and Technology, Central 5, 1-1-1 Higashi, Tsukuba, Ibaraki 305-8565, Japan*

† Electronic supplementary information (ESI) available: Electronic polarization directly induced by external electric field; geometrical structures; Cartesian coordinates of optimized structures. See DOI: https://doi.org/10.1039/d3cp00577a

formula for evaluating the energy profile under an external EF. This formula is applied to the PT process that includes numerous chemical bond formations and dissociations under external EFs. We reveal the atomic-scale mechanism of PT on the surface depending on the direction and intensity of the external EFs.

Theoretical methods

The central purpose of this study is to elucidate the EF effect on a heterogeneous material, as shown in Fig. 1.[6–9] The steam reforming reaction of hydrocarbons was experimentally studied using the system illustrated in Fig. 1, where water vapor (*i.e.*, not aqueous solution) was supplied.[6,8,9] This system is regarded as a complex one because a small electric current can induce a wide variation in the resulting direction and intensity of the gross EF owing to EFs generated by electronic polarization of the constituents. Therefore, the Berry phase theory[13,14] was used to investigate the effect of external EFs with various orientations toward the material surface. We calculated the difference in the macroscopic polarization $\Delta\mathbf{P}$ caused by changes in the geometrical structure during the PT process, where the macroscopic polarization $\mathbf{P}$ is the dipole moment per unit volume. Subsequently, we evaluated the energy change ΔE depending on an external EF using the formula:

$$\Delta E(\boldsymbol{\varepsilon}) = \Delta E(\boldsymbol{\varepsilon} = \mathbf{0}) - \Omega\Delta\mathbf{P}\cdot\boldsymbol{\varepsilon} \quad (1)$$

where $\boldsymbol{\varepsilon}$ is the EF, Ω is the cell volume, $\Delta E(\boldsymbol{\varepsilon} = \mathbf{0})$ is the energy change when the EF is absent, and $-\Omega\Delta\mathbf{P}\cdot\boldsymbol{\varepsilon}$ is the change in the potential energy due to the electrostatic interaction between the EF and the material. $\Delta\mathbf{P}$ is caused by the displacement of charged atomic species and the change in the electron density distribution; thus, the formula can be used to reveal the effect of an EF on various chemical processes. Furthermore, because the EF is considered an additional parameter, a wide range of EF magnitudes and the corresponding energy changes can be examined. Using this approach, we considered a wide range of intensities for the applied EFs that point in arbitrary directions to the material surface.

Our approach assumes that electronic polarization directly induced by the EF can be neglected. This assumption is valid within the context of this study owing to the low-magnitude EF that is used (less than 2×10^9 V m^{-1}). A detailed discussion is provided in Section S1 in the ESI.†

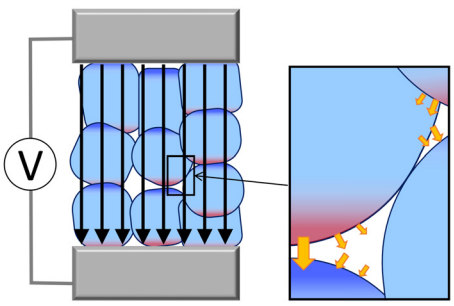

Fig. 1 External electric fields (black arrows) generated by electrodes (gray) in a heterogeneous material (cyan) with complex interfaces. The red and blue colors represent electronic polarization of the system that changes the distribution of the EFs (orange arrows).

Computational details

DFT calculations were performed using the Quantum Espresso program[19] with the dispersion-corrected PBE functional (PBE-D2)[20–23] and the projector augmented wave (PAW) pseudopotential.[24] The cell volume was 3.78 × 10.43 × 30.00 Å^3 along the x ([0$\bar{1}$0]), y ([10$\bar{1}$]), and z ([101]) directions, respectively. The cutoff energies for the wave function and electron density were 62 and 600 Ry, respectively. The number of k-points was 3 × 1 × 1 for the geometry optimization and the Nudged Elastic Band (NEB)[25] calculation, and 9 × 6 × 3 for the Berry phase calculation to confirm the convergence of the Berry phase with respect to the number of k-points. Geometry optimizations in the NEB calculation were performed until the forces were less than 0.05 eV Å^{-1}. The VESTA program was used to visualize the electron density.[26]

Fig. 2 shows the H_2O/TiO_2 system in which water molecules are adsorbed on the stoichiometric anatase (101) surface. The H_2O/anatase (101) interface has been widely studied experimentally and theoretically.[27–34] In Fig. 2(b), the black line indicates a unit cell containing two water molecules. The surface water coverage of the present system corresponds to the water monolayer on the surface investigated in previous studies.[30–33] The geometric structure of the bottom two O–Ti–O trilayers is fixed to that of the bulk anatase. The oxygen atoms of the water molecules (O_w) are bound to the undercoordinated

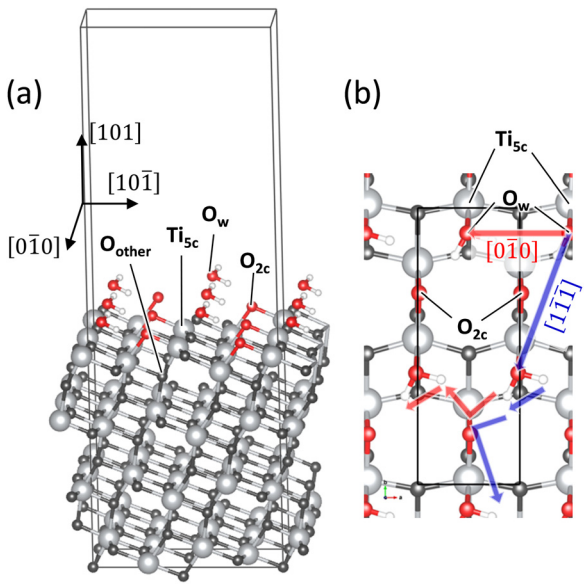

Fig. 2 (a) Bird's-eye view of the H_2O/TiO_2 system. (b) Top view of the system where the directions of the PT investigated in this study are depicted. Ti and H atoms are shown with light grey balls and smaller white balls, respectively. 2-Fold oxygens (O_{2c}) in the surface and water oxygens (O_w) are shown with red balls, and other oxygens (O_{other}) are shown with dark grey balls. The black rectangle in (b) shows the first trilayer of the super cell containing 16 TiO_2 units employed in this study. (a) includes more than three super cells for visibility of the surface structure.

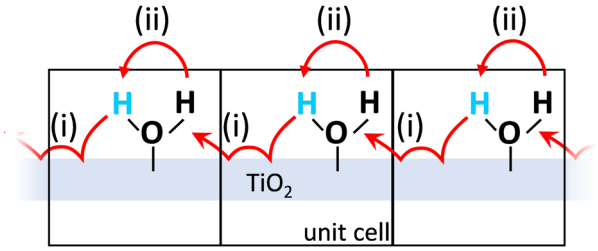

Fig. 3 Scheme of the PT investigated in this study. The cyan H atoms are identical under the periodic boundary condition.

5-fold Ti atoms (Ti_{5c}) on the surface, and the O_w–H bonds point toward the surface undercoordinated 2-fold oxygen atoms (O_{2c}) due to the H···O_{2c} hydrogen bonds. The orientation of the monolayer H_2O molecules was governed by the hydrogen bond, as previously reported.[32]

TiO_2 surfaces other than the anatase (101) are not examined in this study because our primary focus is on the EF effect depending on the direction and magnitude of the applied EF. An H_2O monolayer was chosen to focus on the PT governed by the interaction between H_2O and the surface; water was assumed to be present as a low-pressure vapor. Previous experimental studies have examined analogous systems consisting of the surface and water vapor that generates a water monolayer or submonolayer on the surface.[31,33,34] Multilayer adsorption on the surface, *i.e.*, the interface between an aqueous solution and the surface, is beyond the scope of this study.

Fig. 3 illustrates the PT mechanism investigated in this study. The H atoms hop between the water molecules and the surface and transfer to the next unit cell (i), followed by the rotation of OH and H_2O moieties (ii). The PT process was traced using the NEB method, and unidirectional PT on the surface was expressed. PT in the $[0\bar{1}0]$ and $[1\bar{1}\bar{1}]$ directions was examined, as shown in Fig. 2(b). Comparing these pathways yields insights into the EF effect governed by the quantum mechanical interactions between water and the surface.

Results and discussion

Fig. 4 shows an energy diagram of the PT on the surface. The PT process primarily comprises proton hoppings and O–H group rotations. These steps are denoted as Hop and Rot, respectively, in Fig. 4, with the PT direction indicated by cyan arrows. The horizontal and vertical directions are $[0\bar{1}0]$ and $[10\bar{1}]$, respectively, as defined in Fig. 2(b). The geometrical structures of the intermediates are shown in Fig. S2 in the ESI.†

The energy diagram of PT along the $[0\bar{1}0]$ direction without an applied EF is shown by the solid black line in Fig. 4(a). Both the R → I1 and I1 → I2 steps are attributed to the proton hopping from O_w to O_{2c} owing to the two water molecules in the unit cell. The O_w–H and O_{2c}–H groups simultaneously rotate in the I2 → $I3_a$ step. The energy diagram is symmetric around $I3_a$ because the geometry change from $I3_a$ to P is almost identical to that from $I3_a$ to R; thus, the states after $I3_a$ are denoted by adding a prime (′) to the corresponding states before $I3_a$. The first hopping process (R → I1) has the highest activation energy (0.55 eV) among the elementary steps. The apparent activation energy is determined by the energy difference between R and TS2 (0.65 eV), whereas TS1 determines the apparent activation energy under the EF. The geometric structure of P is equivalent to that of R, except that the sum of transferred distance of the two H atoms in each H_2O molecule is one unit cell length. Therefore, the energies of R and P are identical, provided an external EF is not applied. However, the symmetry in the energy profiles is broken with the applied EF; thus, R and P are no longer energetically equivalent.

Fig. 4(b) shows the energy diagram for PT along the $[1\bar{1}\bar{1}]$ direction. The steps from R to I2 are identical to those shown in Fig. 4(a). PT along the $[10\bar{1}]$ direction occurs through the I2 → $I3_b$ and $I3_b$ → P steps, with the two H_2O_w moieties rotating in the $I3_b$ → P step. TS1 exhibits the largest activation energy for an elementary step (0.55 eV), although $TS3_b$ has a comparable energy of 0.52 eV. The apparent activation energy is determined by $TS3_b$ and is 0.80 eV.

Fig. 5 illustrates the geometrical structures of the major transition states, TS1 and $TS3_b$. The black arrows indicate the transferred H atoms. In both the transition states, the transferred H atom bridges O_w and O_{2c}, and the O_w atom is bound to a Ti_{5c} atom. The O_w–Ti_{5c} bond distance changes from 2.33 Å (R) to 1.85 Å (I1) *via* TS1 and from 1.87 Å (I2) to 2.35 Å ($I3_b$) *via* $TS3_b$, indicating the formation and dissociation of the O_w–Ti_{5c} chemical bond during this process. The O_w–Ti_{5c} bond is strongly distorted in the transition states due to the O_w···H···O_{2c} bonds; that is, the transition states include proton hopping and geometric distortion of the TiO_2 surface. The calculation shows that the atomic-scale details of the bond rearrangement at the interface between water molecules and the surface govern the transition states of the PT. Atomic-scale insights are essential for understanding the EF effect on the energy profile.

Fig. 4 shows the energy diagram for a 10^9 V m^{-1} applied EF, which corresponds to the typical EF intensity generated in electric double layers.[2] The present study mainly focuses on the interface between the surface and water vapor (*i.e.*, not aqueous solution), generating a water monolayer or submonolayer on the surface. The 10^9 V m^{-1} EF is approximately 10 000 times stronger than the external EF used by Sekine *et al.*, where water vapor was used for the steam reforming reaction of hydrocarbons.[6,35] However, if heterogeneous interfaces generate strong EFs owing to the enhancement of electronic polarization by the small electric current (Fig. 1), the theoretical system corresponds to the experimental system. A direct comparison between the present theoretical result and experiment is difficult because the local EF intensity in the experimental system cannot be adequately measured because of its complexity. However, at least, PT on various metal-oxide species under EFs was investigated in the experimental studies.[6,8,9,35]

The solid red line in Fig. 4(a) shows the energy diagram under an EF applied in the $[0\bar{1}0]$ direction. The energies decrease, particularly in the R → I1 and I1 → I2 steps, and the activation energy of the PT in TS1 decreases by 0.09 eV.

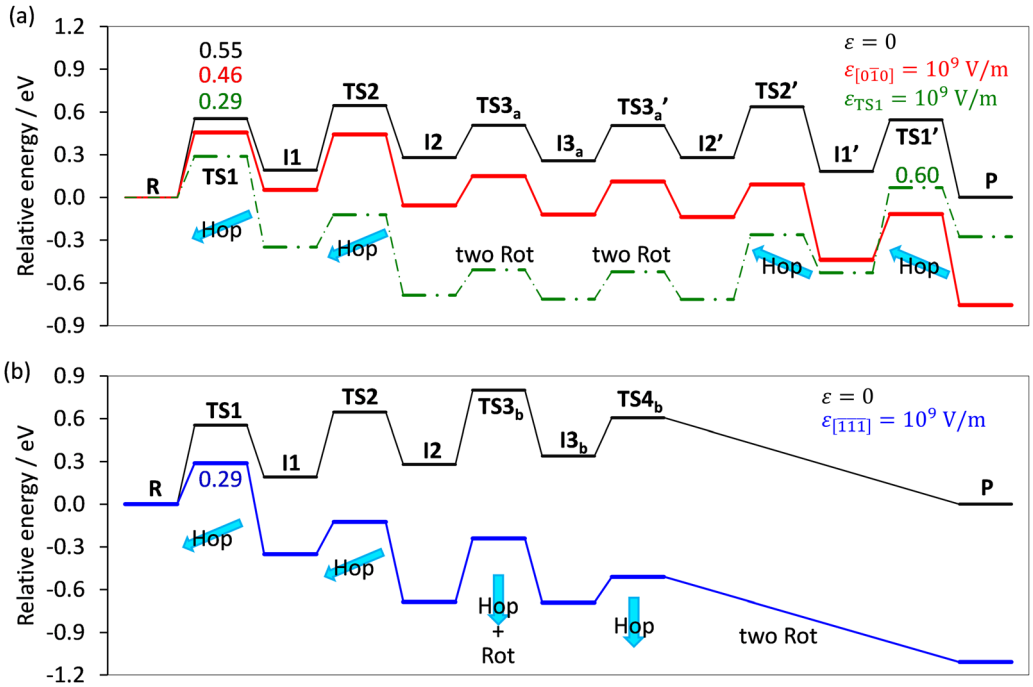

Fig. 4 Energy diagram of the PT toward the (a) [0$\bar{1}$0] and (b) [1$\bar{1}\bar{1}$] directions. The direction of the PT is schematically illustrated with cyan arrows. The solid black and red (blue) lines are the results without an external EF and of applying 10^9 V m^{-1} EF along the [0$\bar{1}$0] ([1$\bar{1}\bar{1}$]) direction, respectively. The dashed green line in (a) is the result of applying 10^9 V m^{-1} EF which decreases the energy of TS1 most.

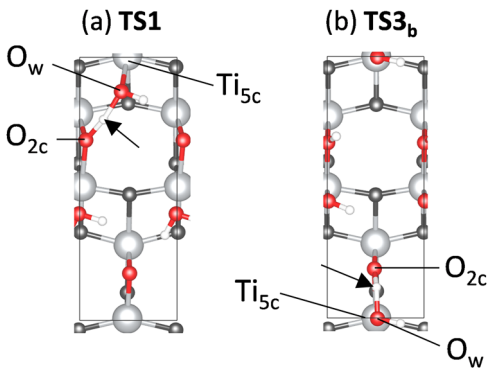

Fig. 5 Geometrical structures of (a) TS1 and (b) $TS3_b$.

The rate-determining step given by the apparent activation energy changes from TS2 to TS1 because TS2 is largely stabilized. The green dashed line in Fig. 4(a) shows the energy diagram for a 10^9 V m^{-1} EF applied parallel to the $\Delta\mathbf{P}$ direction during the R → TS1 step. The barrier to TS1 decreases substantially because the parallel alignment of $\boldsymbol{\varepsilon}$ and $\Delta\mathbf{P}$ yields a large energy change, defined by $\Delta\mathbf{P}\cdot\boldsymbol{\varepsilon}$ (eqn (1)). In contrast, the TS1′ barrier increases, indicating that the EF direction should coincide with the net direction of PT rather than the $\Delta\mathbf{P}$ direction during the R → TS1 step to efficiently induce unidirectional PT along the [0$\bar{1}$0] pathway. We have also investigated the application of an EF along the [010] direction (Fig. S3 in the ESI†), showing that the PT along the [0$\bar{1}$0] direction becomes endothermic by the applied EF. The dependence of the activation energy on the EF direction indicates that the EF effect cannot be explained by considering only one elementary step because the change in energy under the EF differs among the various steps.

The external EF also promotes PT along the [1$\bar{1}\bar{1}$] pathway when the EF is applied in the [1$\bar{1}\bar{1}$] direction. The corresponding energy diagram is indicated by the blue line in Fig. 4(b). Compared with the energy profile without the EF (black line), the activation energy at TS1 markedly decreases from 0.55 to 0.29 eV, whereas that at $TS3_b$ remains almost unchanged. Therefore, $TS3_b$ is the rate-determining step, regardless of external EF application.

This study mainly focuses on the effect of the parallel EFs. The energy change when the EF is perpendicular to the surface was also examined and was significantly smaller (10–30 times) than any of those with the parallel EFs.

Fig. 6 shows the dependence of activation energy in the elementary steps TS1, $TS3_a$, and $TS3_b$ on the magnitude of the EF $|\boldsymbol{\varepsilon}|$. TS1 is common to the [0$\bar{1}$0] and [1$\bar{1}\bar{1}$] pathways. However, the EF direction differs between them. The results shown in Fig. 6 were interpolated; however, the calculations for different field strengths yield identical results when using the present formula (eqn (1)) that neglects the polarization induced by the applied EF. As shown in Fig. 6, the TS1 plots share the same *y*-intercept, but their gradients with respect to $|\boldsymbol{\varepsilon}|$ are different. The direction of $\Delta\mathbf{P}$ in TS1 is closer to [1$\bar{1}\bar{1}$] than [0$\bar{1}$0]; therefore, the gradient for the [1$\bar{1}\bar{1}$] process is steeper than that for the [0$\bar{1}$0] process. The order of the magnitude of the activation energies depends on the EF. When $|\boldsymbol{\varepsilon}|$ is less than

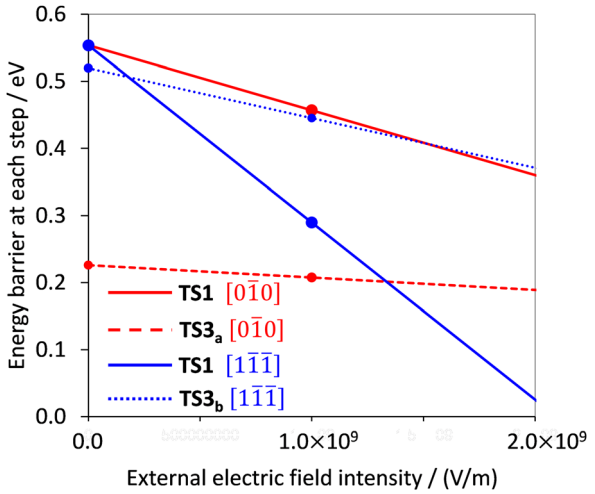

Fig. 6 Dependence of the activation energy of elementary steps on the EF. The energy shown in Fig. 4 is indicated by the circle marker.

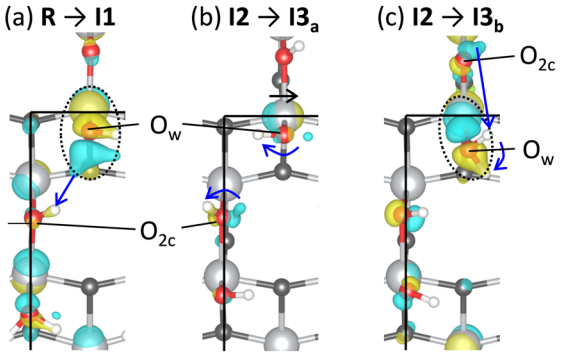

Fig. 8 Variation in the electron density. The increase and decrease in the electron density are illustrated with yellow and cyan, respectively. The threshold of the density is set to the same value for comparison. The colors of atoms are the same as those of Fig. 2. For example, in (a), the electron density difference between R and I1 is superimposed on the geometrical structure of I1.

1.4×10^9 V m^{-1}, TS1 in the [0$\bar{1}$0] pathway exhibits the highest activation energy. When $|\varepsilon|$ is between 1.4×10^9 V m^{-1} and 2.0×10^9 V m^{-1}, the activation energy of $TS3_b$ in the [1$\bar{1}\bar{1}$] pathway is the highest. This variation suggests that the preferred PT pathway depends on the EF magnitude. The energy diagram profiles vary qualitatively owing to differences in the EF dependence among the elementary steps.

As per eqn (1), the energy change *versus* EF is determined by $\Delta\mathbf{P}\cdot\boldsymbol{\varepsilon}$. Thus, the displacement of the H atom, $\Delta\mathbf{r}_H$, can provide a large contribution to $\Delta\mathbf{P}$. Fig. 7 summarizes the direction and magnitude of $\Delta\mathbf{P}$ and $\Delta\mathbf{r}_H$ for the major transition states (TS1, $TS3_a$, and $TS3_b$). The black arrows reflect the exact magnitudes and directions of $\Delta\mathbf{P}$ and $\Delta\mathbf{r}_H$. The horizontal and vertical directions are [0$\bar{1}$0] and [10$\bar{1}$], respectively, as defined in Fig. 2(b). No clear correlation between $\Delta\mathbf{P}$ and $\Delta\mathbf{r}_H$ is evident, indicating that $\Delta\mathbf{P}$ cannot be evaluated solely using $\Delta\mathbf{r}_H$. Therefore, the variation in the activation energy with EF (Fig. 4 and 6) is significantly different from that determined by the classical electric work of an EF carrying a point charge. A previous theoretical study on oxygen-charged defects in MgO and SiO_2 indicated that the effective polarization-work charge under an EF is not equal to the transported charge of the migrating atom.[36]

(a)	R	TS1	I1	I2	$TS3_a$	$I3_a$
$\Delta\mathbf{P}$		↓	↓		↓	↑
$\Delta P_{[0\bar{1}0]}$		0.013	0.006		0.003	0.003
$\Delta\mathbf{r}_H$		↙	←		↙	↖
$\Delta r_{H,[0\bar{1}0]}$		0.65	0.52		1.35	1.51

(b)	R	TS1	I1	I2	$TS3_b$	$I3_b$
$\Delta\mathbf{P}$		↓	↓		↓	~ 0
$\Delta P_{[1\bar{1}\bar{1}]}$		0.036	0.038		0.010	-0.001
$\Delta\mathbf{r}_H$		↙	←		↙	↓
$\Delta r_{H,[1\bar{1}\bar{1}]}$		0.90	0.27		1.21	2.97

Fig. 7 Variation in the polarization $\Delta\mathbf{P}$ and the displacement of the H atom $\Delta\mathbf{r}_H$ in respective elementary steps for the (a) [0$\bar{1}$0] and (b) [1$\bar{1}\bar{1}$] pathways. The magnitudes of $\Delta\mathbf{P}$/(C m^{-2}) and $\Delta\mathbf{r}_H$/Å along the direction of the applied EF are also shown. The horizontal and vertical directions are the [0$\bar{1}$0] and [10$\bar{1}$] directions, respectively.

The change in the atomic charge of the migrating H atoms (Δq_H) can influence $\Delta\mathbf{P}$. Bader charge analysis indicated that the charges on the H atoms remained almost unchanged during the PT process: 0.57–0.66e and 0.61–0.65e for the [0$\bar{1}$0] and [1$\bar{1}\bar{1}$] pathways, respectively, indicating that the contribution of Δq_H is negligible.

To elucidate the dependence of the energy profile on the EF, we analyzed the PT mechanism at the atomic scale. Fig. 8(a)–(c) show the variation in the electron density during the elementary steps passing through the transition states shown in Fig. 7. The variation was defined as the difference in electron density between the two intermediate states. The variation in electron density is superimposed on the geometrical structure of the intermediate state immediately after the corresponding transition state. Fig. 8(a) shows the R → I1 step passing through TS1, where the H–O_w bond is dissociated, and the O_{2c}–H bond is formed. A large variation in the electron density is observed around the Ti–O_w–H moiety (black dotted circle) due to the PT (blue arrow). The mechanism of the electron density variation is illustrated in Fig. 9(a). The H–O_w bond dissociates (green dashed line) owing to the PT (blue arrow). Subsequently, the electron density in the Ti–O_w moiety (orange bar) increases, owing to the change from physisorption to chemisorption in the Ti–O_w interaction as the bond distance decreases from 2.33 Å to 1.85 Å. Overall, the chemical bond rearrangement in

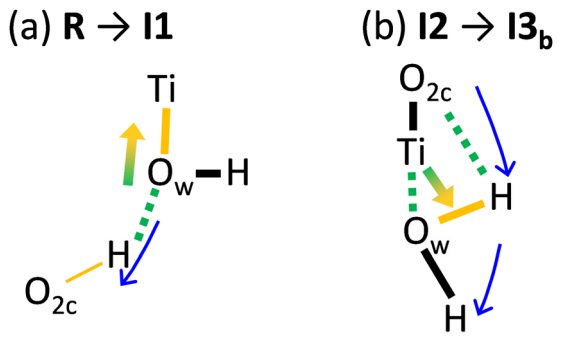

Fig. 9 Scheme of polarization caused by the chemical bond rearrangement between a H_2O moiety and a Ti_{5c} in the (a) R → I1 and (b) I2 → $I3_b$ steps. The green and yellow bars indicate the dissociated and created chemical bonds, respectively, *via* the PT denoted by the blue arrow. The arrow with green-orange gradient color indicates the direction of the charge transfer.

the Ti–O_w–H–O_{2c} moiety causes electron transfer from the H–O_w moiety to the O_w–Ti moiety (green-orange arrow in Fig. 9(a)). The electron and proton transfers occur in opposing directions; thus, the total polarization increases, as shown in Fig. 7.

Fig. 8(b) illustrates the I2 → $I3_a$ step (passing through $TS3_a$) in which the simultaneous rotations of the O_w–H and O_{2c}–H groups occur. Compared with Fig. 8(a), the variation in the electron density is small because chemical bond rearrangement does not occur. The Ti atom bound to the O_w–H group moves 0.11 Å in the direction (black arrows) opposite to that of the PT (blue arrows). Geometric distortion due to the Ti–O_w bond and hydrogen bonding between the H and the O_w in the next unit cell causes stress, which results in the movement of the Ti atom. The polarizations caused by the Ti displacement and PT cancel each other, resulting in a small total variation in $\Delta\mathbf{P}$ in the I2 → $I3_a$ step despite $\Delta\mathbf{r}_H$ in the I2 → $I3_a$ step being larger than that in the R → I1 step (Fig. 7). These results reveal the significance of geometry changes in the H_2O moiety and the surface in the EF effect on the PT.

Fig. 8(c) illustrates the I2 → $I3_b$ step (passing through $TS3_b$), and Fig. 9(b) illustrates the corresponding polarization mechanism. In this step, the H–O_{2c} bond is dissociated and the O_w–H bond is formed, followed by rotations of the regenerated H_2O_w moiety. The Ti–O_w bond is broken during the PT as the bond length increases from 1.87 Å to 2.35 Å. Therefore, electron density in the Ti–O_w region decreases. Overall, the electronic charge is transferred from the Ti–O_w to the O_w–H region, as depicted by the green-orange arrow in Fig. 9(b). In this step, the amount of polarization is governed by the bond dissociation at the O_{2c}–H and Ti–O_w moieties and the O_w–H bond formation. The resultant polarizations cancel each other, and the net polarization is small, as shown in Fig. 7. The mechanisms illustrated in Fig. 9 do not fit the classical charge transfer model. The amount of polarization is determined by the rearrangement of the chemical bond network at the interface between the water molecules and the surface, and quantum mechanical interactions at the interface region govern the EF effect on the energy profile of the PT.

Conclusion

We studied the EF effect on PT on a metal oxide surface using the first-principles computational method. The Berry phase theory was used to calculate the polarization, and we elucidated the dependence of the PT energy profile on the direction and magnitude of the EF. The variation in the polarization was notable during the O_w–H bond dissociation, which was significantly enhanced by the EF. No clear correlation exists between the polarization and displacement of H atoms, indicating that the polarization cannot be explained as the classical electric work of an EF carrying a point charge. The variation in the electron density reveals that the charge transfer in the PT is caused by the chemical bond rearrangement at the interface between the water molecules and the surface; that is, the quantum mechanical interaction at the interface region governs the EF effect on the PT energy profile. Furthermore, the non-negligible contribution of the geometric distortion of the surface to the EF effect infers the importance of the metal oxide species on which PTs take place. Because of the low computational cost for evaluating the EF effect, the present method is a potential candidate for investigations of more complex systems, such as the interface between an aqueous solution and the surface at which the route of PT may be diverse. In this regard, this study presents the theoretical approach to investigate the EF effect on various chemical processes in which the distribution of the EF is non-uniform in space with respect to material surfaces.

Author contributions

K. I. and S. F. planned the research. T. C., K. I., and J. H. wrote the manuscript. T. C. performed the calculations. All authors have checked the manuscript.

Conflicts of interest

There are no conflicts to declare.

Acknowledgements

This study was financially supported by JSPS KAKENHI (grant no. 19K15513 and JP20H02685) and the Collaborative Research Program of the Institute for Chemical Research, Kyoto University (grant no. 2022-61). This work was also supported by the MEXT project ''Integrated Research Consortium on Chemical Sciences'' and the Photo-excitonix Project of Hokkaido University. Most of the theoretical computations were performed using the computational resources of the Grand Chariot supercomputer provided by Hokkaido University through the HPCI System Research Project (Project ID: hp220135). Some of the computations were performed at the RCCS (Okazaki, Japan, Project: 22-IMS-C002), Super Computer System, Institute for Chemical Research (Kyoto University), and ACCMS (Kyoto University).

References

1 G. Karlberg, J. Rossmeisl and J. K. Nørskov, *Phys. Chem. Chem. Phys.*, 2007, **9**, 5158.
2 C. F. Gorin, E. S. Beh and M. W. Kanan, *J. Am. Chem. Soc.*, 2012, **134**, 186–189.
3 C. Aragones, N. L. Haworth, N. Darwish, S. Ciampi, N. J. Bloomfield, G. G. Wallace, I. Diez-Perez and M. L. Coote, *Nature*, 2016, **531**, 88–91.
4 S. Shaik, D. Mandal and R. Ramanan, *Nat. Chem.*, 2016, **8**, 1091–1098.
5 T. Stuyver, D. Danovich, J. Joy and S. Shaik, *Wiley Interdiscip. Rev.: Comput. Mol. Sci.*, 2020, **10**, e1438.
6 Y. Sekine, M. Haraguchi, M. Matsukata and E. Kikuchi, *Catal. Today*, 2011, **171**, 116–125.
7 S. Ø. Stub, E. Vøllestad and T. Norby, *J. Mater. Chem. A*, 2018, **6**, 8265–8270.
8 R. Manabe, S. Okada, R. Inagaki, K. Oshima, S. Ogo and Y. Sekine, *Sci. Rep.*, 2016, **6**, 1–7.
9 K. Takise, A. Sato, S. Ogo, J. G. Seo, K.-I. Imagawa, S. Kado and Y. Sekine, *RSC Adv.*, 2019, **9**, 27743–27748.
10 J. Neugebauer and M. Scheffler, *Phys. Rev. B: Condens. Matter Mater. Phys.*, 1992, **46**, 16067.
11 M. P. Hyman and J. W. Medlin, *J. Phys. Chem. B*, 2005, **109**, 6304.
12 P. Deshlahra, E. E. Wolf and W. F. Schneider, *J. Phys. Chem. A*, 2009, **113**, 4125.
13 R. King-Smith and D. Vanderbilt, *Phys. Rev. B: Condens. Matter Mater. Phys.*, 1993, **47**, 1651.
14 R. Resta, *Rev. Mod. Phys.*, 1994, **66**, 899.
15 R. Resta and D. Vanderbilt, *Physics of Ferroelectrics: A Modern Perspective*, Springer Berlin Heidelberg, Berlin, Heidelberg, 2007, pp. 31–68.
16 Z. Futera and N. J. English, *J. Phys. Chem. C*, 2016, **120**, 19603–19612.
17 C. Dette, M. A. Perez-Osorio, S. Mangel, F. Giustino, S. J. Jung and K. Kern, *J. Phys. Chem. C*, 2017, **121**, 1182–1187.
18 M. Zhou and H. Wang, *JACS Au*, 2021, **2**, 188–196.
19 P. Giannozzi, S. Baroni, N. Bonini, M. Calandra, R. Car, C. Cavazzoni, D. Ceresoli, G. L. Chiarotti, M. Cococcioni and I. Dabo, *et al.*, *J. Phys.: Condens. Matter*, 2009, **21**, 395502.
20 J. P. Perdew, K. Burke and M. Ernzerhof, *Phys. Rev. Lett.*, 1996, **77**, 3865–3868.
21 J. P. Perdew, K. Burke and M. Ernzerhof, *Phys. Rev. Lett.*, 1997, **78**, 1396.
22 S. Grimme, *J. Comput. Chem.*, 2006, **27**, 1787.
23 V. Barone, M. Casarin, D. Forrer, M. Pavone, M. Sambi and A. Vittadini, *J. Comput. Chem.*, 2009, **30**, 934.
24 P. E. Blöchl, *Phys. Rev. B: Condens. Matter Mater. Phys.*, 1994, **50**, 17953.
25 G. Henkelman, B. P. Uberuaga and H. Jónsson, *J. Chem. Phys.*, 2000, **113**, 9901–9904.
26 K. Momma and F. Izumi, *J. Appl. Crystallogr.*, 2011, **44**, 1272.
27 A. Vittadini, A. Selloni, F. P. Rotzinger and M. Grätzel, *Phys. Rev. Lett.*, 1998, **81**, 2954–2957.
28 Y. He, A. Tilocca, O. Dulub, A. Selloni and U. Diebold, *Nat. Mater.*, 2009, **8**, 585–589.
29 C. Sun, L.-M. Liu, A. Selloni, G. Q. M. Lu and S. C. Smith, *J. Mater. Chem.*, 2010, **20**, 10319–10334.
30 H. Sun, D. J. Mowbray, A. Migani, J. Zhao, H. Petek and A. Rubio, *ACS Catal.*, 2015, **5**, 4242–4254.
31 L. E. Walle, A. Borg, E. M. J. Johansson, S. Plogmaker, H. Rensmo, P. Uvdal and A. Sandell, *J. Phys. Chem. C*, 2011, **115**, 9545–9550.
32 A. Tilocca and A. Selloni, *Langmuir*, 2004, **20**, 8379–8384.
33 G. S. Herman, Z. Dohnálek, N. Ruzycki and U. Diebold, *J. Phys. Chem. B*, 2003, **107**, 2788–2795.
34 K. Shirai, T. Sugimoto, K. Watanabe, M. Haruta, H. Kurata and Y. Matsumoto, *Nano Lett.*, 2016, **16**, 1323–1327.
35 T. Yabe and Y. Sekine, *Fuel Process. Technol.*, 2018, **181**, 187–198.
36 N. Salles, L. Martin-Samos, S. De Gironcoli, L. Giacomazzi, M. Valant, A. Hémeryck, P. Blaise, B. Sklenard and N. Richard, *Nat. Commun.*, 2020, **11**, 1–7.